




Probing the Morphology of Polarized Emission Induced by Fluctuation Dynamo Using Minkowski Functionals

Riju Dutta¹ , Sharanya Sur² , and Aritra Basu^{3,4} ¹ Department of Physics, Indian Institute of Science, Bangalore 560012, India² Indian Institute of Astrophysics, 2nd Block, Koramangala, Bangalore 560034, India; sharanya.sur@iiap.res.in³ Thüringer Landessternwarte, Sternwarte 5, D-07778 Tautenburg, Germany⁴ Max-Planck-Institut für Radioastronomie, Auf dem Hügel 69, D-53121 Bonn, Germany

Received 2024 March 26; revised 2024 October 17; accepted 2024 October 17; published 2024 November 21

Abstract

The morphology and the characteristic scale of polarized structures provide crucial insights into the mechanisms that drive turbulence and maintain magnetic fields in magneto-ionic plasma. We aim to establish the efficacy of Minkowski functionals as quantitative statistical probes of filamentary morphology of polarized synchrotron emission resulting from fluctuation dynamo action. Using synthetic observations generated from magnetohydrodynamic simulations of fluctuation dynamos with varying driving scales (ℓ_f) of turbulence in isothermal, incompressible, and subsonic media, we study the relation between different morphological measures and their connection to fractional polarization (p_f). We find that Faraday depolarization at low frequencies gives rise to small-scale polarized structures that have higher filamentarity as compared to the intrinsic structures that are comparable to ℓ_f . Above ~ 3 GHz, the number of connected polarized structures per unit area ($N_{CC,peak}$) is related to the mean p_f ($\langle p_f \rangle$) of the emitting region as $\langle p_f \rangle \propto N_{CC,peak}^{-1/4}$, provided the scale of the detectable emitting region is larger than ℓ_f . This implies that $N_{CC,peak}$ represents the number of turbulent cells projected on the plane of the sky and can be directly used to infer ℓ_f via the relation $\ell_f \propto N_{CC,peak}^{-1/2}$. An estimate of ℓ_f thus directly allows for pinning down the turbulence-driving mechanism in astrophysical systems. While the simulated conditions are mostly prevalent in the intracluster medium of galaxy clusters, the qualitative morphological features are also applicable in the context of interstellar medium in galaxies.

Unified Astronomy Thesaurus concepts: [Magnetohydrodynamics \(1964\)](#); [Magnetohydrodynamical simulations \(1966\)](#); [Magnetic fields \(994\)](#); [Galaxy clusters \(584\)](#); [Intracluster medium \(858\)](#); [Radio astronomy \(1338\)](#); [Spectropolarimetry \(1973\)](#)

1. Introduction

Magnetic fields are pervasive in almost all astrophysical objects in our Universe and are believed to be amplified and maintained by some form of dynamo action (see P. Charbonneau 2014; A. M. Shukurov & K. Subramanian 2021 for reviews). Polarization observations of magnetic fields in turbulent media probe the 2D projection of the ordered and random component of the fields in the plane of the sky. Along with information on Faraday depth that probes the magnetic field component parallel to the line of sight (LOS), rudimentary insight into the 3D structure of magnetic fields can be obtained under certain assumptions (R. Beck 2015). Such measurements are often challenging to interpret (A. Basu et al. 2019), and therefore, directly connecting them to the intrinsic magnetic field morphology and its 3D statistical properties is rather arduous.

In the majority of astrophysical systems, where the bulk of the diffuse media are turbulent, fast, and efficient, *fluctuation dynamos* are believed to amplify and maintain magnetic fields (A. P. Kazantsev 1968; F. Rincon 2019; A. M. Shukurov & K. Subramanian 2021). These dynamos are capable of amplifying weak, initial seed magnetic fields embedded in a conducting fluid to near-equipartition strengths by 3D turbulent flows (e.g., N. E. Haugen et al. 2004; A. A. Schekochihin et al. 2004a; J. Cho et al. 2009; P. Bhat & K. Subramanian 2013; C. Federrath 2016;

S. Xu & A. Lazarian 2016, 2021; A. Seta et al. 2020; S. Sur & K. Subramanian 2024). The morphology of magnetic fields generated by these dynamos and the associated emission, e.g., via the synchrotron mechanism, are intermittent, strongly non-Gaussian, wherein the characteristic emission scale depends on the driving scale of turbulence (A. Basu & S. Sur 2021; S. Sur et al. 2021). It is therefore imperative to quantify the nature of polarized structures in order to glean information on the underlying mechanism of magnetic field amplification.

In recent times, intensity gradient techniques (B. M. Gaensler et al. 2011; Y. Hu et al. 2019; L. Carmo et al. 2020; R.-Y. Wang et al. 2021) and statistical correlation functions (M. Haverkom et al. 2008; S. Mao et al. 2015; M. Nandakumar & P. Dutta 2020; A. Seta et al. 2023) have been used to infer the statistical properties of turbulent magneto-ionic media. While intensity gradient techniques provide insights into the alignment of the magnetic field with various observational tracers, quantitative interpretations often rely on benchmarking against numerical simulations. On the other hand, statistical correlation functions are mostly insensitive to the morphology of the structures (A. Seta et al. 2018). In this work, we study the 2D morphological properties of synthetic polarized synchrotron emission produced by fluctuation dynamos driven on different scales using quantitative morphological measures based on *Minkowski functionals* (R. J. Adler & J. E. Taylor 2007). This technique provides morphological description of any structure in N -dimensions and has been extensively used to study the morphological features in cosmological large-scale structures (e.g., K. R. Mecke et al. 1994; V. Sahni et al. 1998; S. Bharadwaj et al. 2000), anisotropy in maps of the cosmic microwave



Original content from this work may be used under the terms of the [Creative Commons Attribution 4.0 licence](#). Any further distribution of this work must maintain attribution to the author(s) and the title of the work, journal citation and DOI.

background (J. Schmalzing & K. M. Gorski 1998), and in quantifying structures of the Galactic H I emission (P. M. W. Kalberla & U. Haud 2023). They have also been used to study the morphology of turbulent fluid flows (E. Calzavari et al. 2008), magnetic field structures in the kinematic (S. L. Wilkin et al. 2007) and nonlinear stages (A. Seta et al. 2020) of fluctuation dynamos, and even those of reconnecting fields (S. Dwivedi et al. 2024) in magnetically dominated decaying turbulence. Recently, they have also been used to infer the shapes of substructures in shocks of radio relics (D. Wittor et al. 2023).

In S. Sur et al. (2021) and A. Basu & S. Sur (2021), we studied in detail the statistical properties of polarized synchrotron emission arising from fluctuation dynamo action in the context of the intracluster medium (ICM), which is both Faraday rotating and synchrotron emitting. In this work, we address for the first time certain key questions that provide crucial insights into the morphology of these polarized structures. With the aid of synthetic maps of the fractional polarization (p_f), we explore how the number of 2D structures varies with p_f and the effects of frequency-dependent Faraday depolarization on the number and filamentarity of these structures when the size of the emission regions are larger compared to the turbulent driving scales (ℓ_f). Additionally, we also explore the effect of emission regions on scales comparable to or smaller than ℓ_f and explore how the morphological features are related to ℓ_f . As we show in this paper, our analysis reveals that Minkowski functionals are effective probes to study the properties of polarized synchrotron emission, and the number of such structures can indeed be used to infer the scale of turbulent motions.

2. Data and Methodology

2.1. Simulations and Synthetic Observations

We use data from three nonideal MHD simulations of fluctuation dynamos reported in A. Basu & S. Sur (2021) where turbulence is driven solenoidally (i.e., $\nabla \cdot \mathbf{F} = 0$, \mathbf{F} is the forcing term) over a range of wavenumbers—(i) $1 \leq |\mathbf{k}|L/2\pi \leq 3$, (ii) $4 \leq |\mathbf{k}|L/2\pi \leq 6$, and (iii) $7 \leq |\mathbf{k}|L/2\pi \leq 9$, as a stochastic Ornstein–Uhlenbeck process with a finite time correlation. Thus, the average forcing wavenumbers are $k_f L/2\pi = 2, 5, \text{ and } 8$, where L is the length of the box. These k_f correspond to turbulent driving scales $\ell_f = 2\pi/k_f = L/2, L/5, \text{ and } L/8$, respectively. We refer the readers to A. Basu & S. Sur (2021), S. Sur et al. (2021), and S. Sur & K. Subramanian (2024) for more details on the basic equations, numerical setup, and initial conditions. In summary, we solve the full set of 3D magnetohydrodynamic equations in dimensionless units on a uniform grid consisting of 512^3 grid points in a periodic box of unit length with an isothermal equation of state using the FLASH code⁵ (V. Eswaran & S. B. Pope 1988; B. Fryxell et al. 2000; R. Benzi et al. 2008) (version 4.2). The amplitude of the driving results in subsonic turbulence with rms Mach number $\mathcal{M} \approx 0.2$. The eddy turnover time at the driving scale is $t_{\text{ed}} = \ell_f/u_{\text{rms}}$, where u_{rms} is the rms value of the turbulent velocity in the steady state. For given values of the physical viscosity (ζ),⁶ we obtain fluid Reynolds number $\text{Re} =$

$u_{\text{rms}}\ell_f/\zeta = 1080, 1450 \text{ and } 1425$ in our simulations with $\ell_f = L/2, L/5, \text{ and } L/8$, respectively. These are large enough to ensure that the flows are turbulent.⁷

Each of the aforementioned simulations was run for several eddy turnover times so as to capture the kinematic, intermediate, and saturated phases of dynamo evolution. The existence of an intermediate phase has been reported in earlier studies (e.g., A. A. Schekochihin et al. 2004b; J. Cho et al. 2009; A. Beresnyak 2012; S. Sur & K. Subramanian 2024). This phase is expected to commence when the magnetic energy density becomes comparable to the kinetic energy density on the smallest supercritical scales and end when the above energy densities become comparable on scales near the outer scale of turbulence (A. M. Shukurov & K. Subramanian 2021). To address the objectives of our study, we solely focus on a number of independent realizations in the saturated phase of the dynamo. This phase is captured over 15, 16, and 20 t_{ed} in simulations with $\ell_f = L/2, L/5, \text{ and } L/8$, respectively. The morphological analysis is then performed by utilizing multiple 3D snapshots of the gas density (ρ) and the three components of the magnetic field (B_x, B_y, B_z) for computing 2D 512×512 pixel maps of the total synchrotron (I), and the polarized synchrotron intensity (PI) in the plane of the sky using the COSMIC package (A. Basu et al. 2019). Physical unit conversion, the choice of the cosmic ray energy spectrum, and normalization for the synchrotron intensity are identical to those described in S. Sur et al. (2021) and A. Basu & S. Sur (2021). We have chosen the x - and y -axes to be in the plane so that the magnetic field component in the plane of the sky $B_{\perp} = (B_x^2 + B_y^2)^{1/2}$ contributes to the total and polarized synchrotron emission, and the component parallel to the LOS, $B_{\parallel} = B_z$, contributes to Faraday rotation. In this work, we will focus on the analysis of 2D maps of fractional polarization (p_f) at a frequency ν , defined as $p_{f,\nu} = \text{PI}_{\nu}/I_{\nu}$, because it is largely independent of our fiducial choice of the normalization of I and the assumed shape of the frequency spectrum. Furthermore, we use synthetic maps at three representative frequencies $\nu = 6, 1, \text{ and } 0.5$ GHz, where the effects of frequency-dependent Faraday depolarization are negligible, moderate, and strong, respectively.

We would like to emphasize that the value of the Faraday rotation measure (RM) and its dispersion (σ_{RM}) depends on the choice of the physical size of the simulation domain L and the free-electron number density (n_e). The synthetic maps of RM have σ_{RM} in the range $90\text{--}120 \text{ rad m}^{-2}$ (A. Basu & S. Sur 2021), and therefore, the frequency dependence of Faraday depolarization would differ for other choices of L and n_e . Although the qualitative results would remain unaffected, the results at 0.5 and 1 GHz should be considered as representative frequencies where Faraday depolarization is high and moderate, respectively. However, all our conclusions are unaffected at $\nu \gtrsim 3$ GHz.

2.2. Computing Minkowski Functionals

To quantify the morphology of 2D structures in the maps of p_f , we computed 2D *Minkowski functionals*—the area (A) and perimeter (P), by developing a new, computationally efficient algorithm implemented via a Python-based software,

⁵ <https://flash.rochester.edu/site/flashcode/>

⁶ Note that performing nonideal MHD simulations is paramount for fluctuation dynamos as this mechanism essentially involves processes close to resistive scales. Hence, we use physical values of viscosity (ν) and resistivity (η) in the momentum and magnetic induction equations, respectively. This is in contrast to ideal MHD simulations where both viscous and resistive dissipation are controlled by numerical diffusion alone.

⁷ Following C. F. McKee et al. (2020), the Reynolds number corresponding to numerical diffusion is $\approx 2N_{\text{grid}}^{4/3} \approx 8000$ for subsonic simulations having $N_{\text{grid}} = 512$ grid points. This implies that explicit diffusion is significantly larger than numerical diffusion in all our runs.

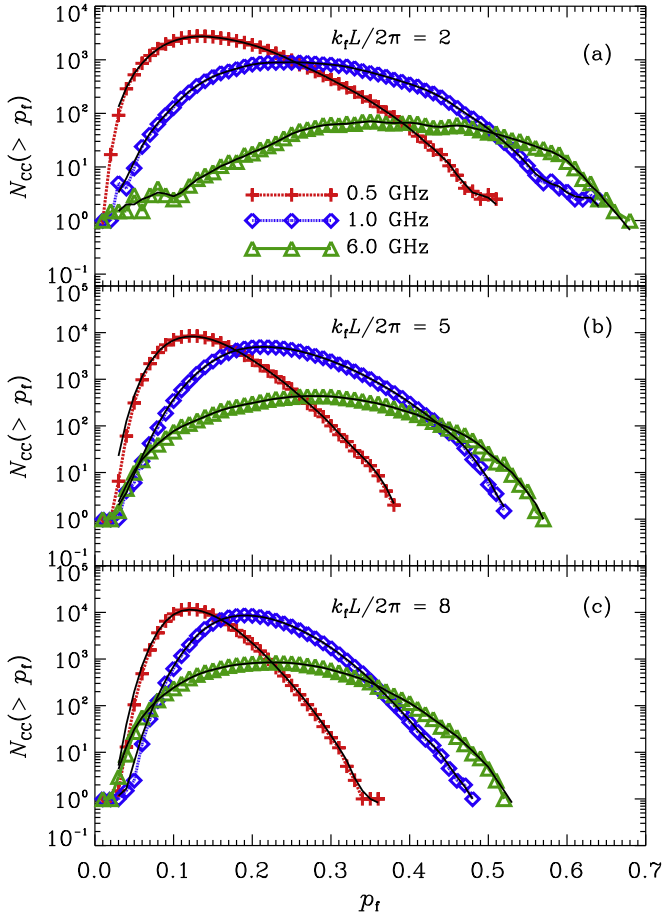


Figure 1. Variation of N_{CC} with the threshold p_f at $\nu = 0.5$ GHz (red, “plus”), 1.0 GHz (blue, “diamond”), and for $\nu = 6.0$ GHz (green, “triangle”) for simulations with different driving scales: $k_f L / 2\pi = 2$ (panel, “(a)”), 5 (panel “(b)”), and 8 (panel “(c)”). The N_{cc} values for each curve were computed over a range of snapshots in the saturated phase of the dynamo in each run. The black solid curves are those obtained by smoothing the data.

perimetrics (R. Dutta et al. 2024).⁸ This is based on the *Marching Squares* algorithm of H. Mantz et al. (2008). The workflow and tests of the algorithm are described in the Appendix. Given A and P , the shape of a structure is quantified in terms of a single dimensionless number, the “filamentarity” (F), defined as,

$$F = \frac{P^2 - 4\pi A}{P^2 + 4\pi A}. \quad (1)$$

The value of F is restricted between 0 and 1, such that $F = 0$ for a circle, and $F = 1$ for a 1D line that can be either straight or curved. This also implies that F is not an additive quantity. Further, it is important to note that, by definition, F is sensitive to the shape of the structures but not to their size. In the following, we study F of 2D maps of p_f for structures above various threshold values of p_f .

3. Results

Utilizing Minkowski functionals, we first compare the morphology of polarized structures generated at varying

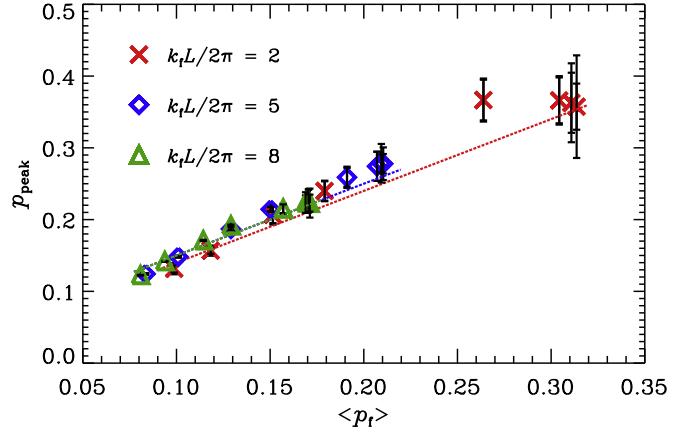


Figure 2. Relation between $\langle p_f \rangle$ and median values of p_{peak} corresponding to $\nu = 0.5, 0.6, 0.8, 1.0, 2.0, 4.0, 5.0,$ and 6.0 GHz (data points from left to right) along with 2σ error bars. Red crosses: $k_f L / 2\pi = 2$, blue diamonds: $k_f L / 2\pi = 5$, and green triangles: $k_f L / 2\pi = 8$. The colored dotted lines represent the 1:1 linear fit to the data.

turbulence driving scales (ℓ_f) and then study the effects of Faraday depolarization on these structures.

3.1. Number of Connected Emitting Components

Using 8-connectivity (R. C. Gonzalez & R. E. Woods 2002), we determine the *connected components* (see Appendix) above a threshold value of p_f from the synthetic maps. This allows us to filter continuous polarized structures above p_f , and compute A and P for each of them. In Figure 1, we show the number of connected components (N_{CC}) above a threshold p_f , $N_{CC}(>p_f)$, as a function of p_f at $\nu = 0.5, 1,$ and 6 GHz as the different symbols, and for the three ℓ_f s as the different panels. For independence, the data points shown in Figure 1 are averaged for two snapshots that are separated by more than t_{ed} . First, we find that, in all cases, $N_{CC}(>p_f)$ peaks for a certain value of p_f , such that the peak is significantly broader at higher frequencies compared to that at lower frequencies. We define p_{peak} as the p_f where $N_{CC}(>p_f)$ is maximum.⁹ Above p_{peak} , N_{CC} decreases rapidly, especially below ≈ 1 GHz. Thus, p_{peak} represents the transition value at which the breaking up of larger structures is balanced by the shrinking and disappearance of smaller structures. Second, irrespective of k_f , the highest number of connected structures, measured in terms of N_{CC} , always occurs at low frequencies, here at 0.5 GHz, for a threshold $p_f \leq 0.15$, close to $\langle p_f \rangle = 0.11$ determined from the p_f map at 0.5 GHz. This is a direct consequence of Faraday depolarization, which gives rise to a plethora of structures at low p_f . Third, at a given frequency, p_{peak} decreases with increasing k_f , similar to what was seen for $\langle p_f \rangle$ in A. Basu & S. Sur (2021).

The physical connection between N_{CC} and p_f can be understood from Figure 2, which shows the variation of p_{peak} with $\langle p_f \rangle$ directly determined from the synthetic maps at different frequencies for all three driving scales. Remarkably, we find that p_{peak} and $\langle p_f \rangle$ closely follow a 1:1 relation (dotted lines in Figure 2), indicating p_{peak} to be a direct measure of $\langle p_f \rangle$ within $\approx 10\%$. However, for $\nu \gtrsim 3$ GHz, both saturate to the value expected for the intrinsic value of $\langle p_f \rangle$ (A. Basu & S. Sur 2021; S. Sur et al. 2021).

⁹ Since the location of p_{peak} could be affected by stochastic variations in N_{CC} , seen as small fluctuations at higher frequencies in Figure 1, we determine p_{peak} by fitting the peak of the top-hat smoothed curves with a parabola.

⁸ doi:10.5281/zenodo.11118211

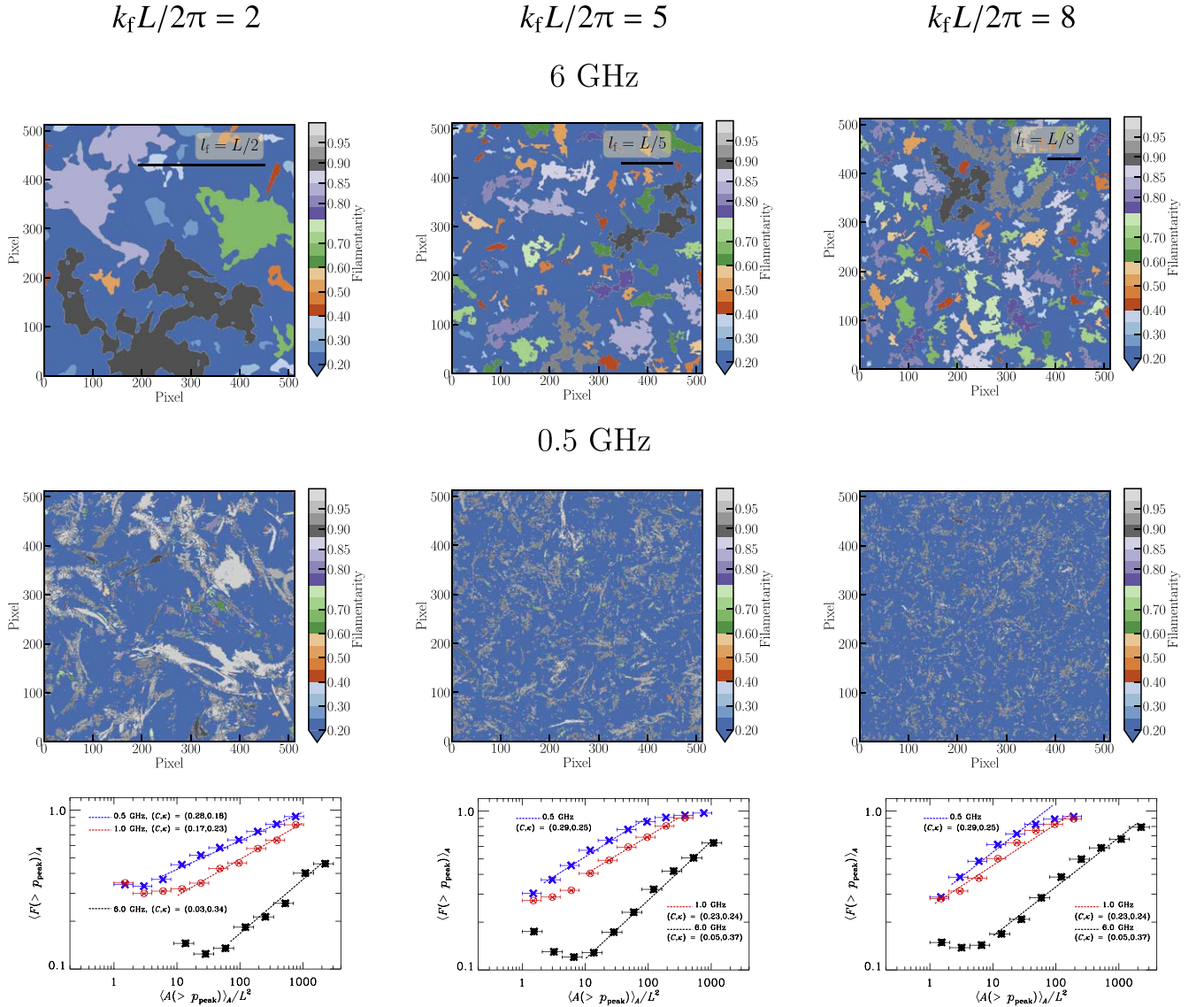


Figure 3. Top and middle rows: maps of filamentarity above the fractional polarization threshold of p_{peak} (see Section 3.1 for details). The top and middle rows are for $\nu = 6$ and 0.5 GHz. Bottom row: variation of average filamentarity in each area bin $\langle F(>p_{\text{peak}}) \rangle_A$ with average area $\langle A(>p_{\text{peak}}) \rangle_A$ binned logarithmically. The dashed lines are linear fits to these curves, for which the x -coordinates are taken to be the bin centers. The left, middle, and right columns are for turbulence driven with $k_t L / 2\pi = 2, 5, \text{ and } 8$, respectively.

3.2. Filamentarity and Sizes of Emitting Components

Here we present the results of the filamentarity of the polarized structures and its dependence on different threshold values of p_f and area A . Note that it is difficult to measure A and P accurately for structures on the scale of the grid points, as they are sensitive to the details of the interpolation and contouring schemes. Hence, we only considered structures having $A > 1$ pixel² throughout this study. Figure 3 shows the map of $F(>p_{\text{peak}})$ at 6 GHz (top row) and 0.5 GHz (middle row) for the three turbulent driving scales. It is apparent that polarized structures with a wide range in F occur in all three cases. For a given k_f , Figure 3 shows that larger structures on scales comparable to l_f with lower F at $\nu = 6$ GHz fragment into smaller structures with higher F at $\nu \lesssim 1$ GHz due to stronger Faraday depolarization at $\nu \lesssim 1$ GHz. This is seen for all choices of the threshold value of p_f . Notably, from these synthetic data, we find the mean filamentarity of all the connected components above a p_f , $\langle F(>p_f) \rangle$, to remain mostly

constant as a function of p_f . In fact, $\langle F(>p_f) \rangle$ is consistently larger with $\langle F \rangle > 0.3$ than that at higher frequencies ($\gtrsim 3$ GHz), where $\langle F \rangle$ lies in the range 0.15–0.22 for all the driving scales, and for all choice of threshold $p_f \gtrsim 0.05$.¹⁰

To see the size dependence of the polarized structures with F , in the bottom row of Figure 3 we show the variation of F averaged within logarithmic bins of A , $\langle F(>p_{\text{peak}}) \rangle_A$, as a function of the mean area $\langle A(>p_{\text{peak}}) \rangle_A$. Here, the subscript “A” represents averaging of the quantities for all connected components whose area, in pixels, lie in the range ΔA^{nK} and $\Delta A^{(n+1)K}$, where $n \in \mathbb{Z}^+$, $K = 0.5$, and $\Delta A = 4$ pixels² for 0.5 and 1 GHz, and $\Delta A = 4.3$ pixels² for 6 GHz. To reduce statistical fluctuations of $\langle F(>p_{\text{peak}}) \rangle_A$, especially in the largest area bins that typically have few connected structures, the data points in Figure 3 (bottom row) are further averaged for two

¹⁰ As seen in Figure 1, the number of N_{CC} at $p_f \lesssim 0.05$ is low for $k_t L / 2\pi = 5$ and 8, and therefore, the variation of $\langle F \rangle$ in this regime is subject to large statistical fluctuations.

independent snapshots that are separated by $>t_{\text{ed}}$. Clearly, as a consequence of increased Faraday depolarization at lower frequencies, $\langle F(>p_{\text{peak}}) \rangle_A$ is larger for all the driving scales for structures spanning a large range in the area. Furthermore, for structures that have $A \gtrsim 10$ pixels², $\langle F(>p_{\text{peak}}) \rangle_A$ varies with $\langle A(>p_{\text{peak}}) \rangle_A$ roughly as a power law, $\langle F(>p_{\text{peak}}) \rangle_A = C \langle A(>p_{\text{peak}}) \rangle_A^\kappa$. The values of the normalization C and power-law index κ are shown in the bottom row of Figure 3. We find κ to lie in the range 0.18 and 0.35, implying large-scale polarized structures to be more filamentary on average. Finally, for $\nu \gtrsim 3$ GHz, where the polarized emission is similar to the intrinsic emission (A. Basu & S. Sur 2021), κ remains roughly the same, $\kappa = 0.31$ – 0.37 , for the three k_f s. However, the normalization C progressively decreases with increasing k_f by more than a factor of 2. This indicates that, for turbulence driven on small scales, the volume-filling polarized structures (A. Basu & S. Sur 2021) are significantly more filamentary. On the other hand, at $\nu \lesssim 1$ GHz, the exponent shows a steady increase from $\kappa = 0.18$ to 0.31, for k_f increasing from 2 to 8. Interestingly, we find indication that, at frequencies where Faraday depolarization is high, e.g., at 0.5 GHz in our case, the area of the largest structures is more than 10 times smaller than those at $\gtrsim 3$ GHz for turbulence driven on small scales.

3.3. Dependence on the Projected Size in the Plane of the Sky

In Sections 3.1 and 3.2, we have performed the morphological analysis for the entire simulated domain, i.e., for the case when polarized emission is detectable over the entire 512×512 pixels² 2D maps. Here, we study the impact on our results for subregions of various sizes (ℓ), especially on the determination of p_{peak} at 6 GHz. This is equivalent to cases where synchrotron emission is detectable only from a fraction of the emitting area, e.g., because of insufficient telescope sensitivity. This allows us to estimate the scales of ℓ at which the linear relationship between p_{peak} and $\langle p_f \rangle$ seen in Figure 2 becomes unreliable. To this end, we sampled multiple regions of size $\ell \times \ell$ in the 2D maps of p_f for ℓ ranging from 25 to 512 pixels. These correspond to ℓ/ℓ_f ranging from 1/8 to 8 for the different k_f . For example, $\ell = 100$ pixels corresponds to an area of $\ell/\ell_f \times \ell/\ell_f \approx 2/5 \times 2/5$ for $k_f L/2\pi = 2$, $\approx 1 \times 1$ for $k_f L/2\pi = 5$, and $\approx 8/5 \times 8/5$ for $k_f L/2\pi = 8$. We chose three different locations for the subregions for each $k_f L/2\pi$, and for the case of $\ell/\ell_f = 2$ for $k_f L/2\pi = 2$, we used two different snapshots in the saturated stages of the turbulent dynamo.

In Figure 4, we show the variation of the relative error on the estimated p_{peak} for different ℓ/ℓ_f as a function of the 95 percentile range, $\Delta p_{\text{peak},95}$, of the p_{peak} determined from Monte Carlo samples.¹¹ Both these quantities are compared relative to $\langle p_f \rangle$ over the entire 512×512 pixel² 2D map. In Figure 4, the y-axis represents the relative deviation in the estimated p_{peak} from the subregions, and the x-axis represents the confidence in the estimated p_{peak} . It is clear that the blueish data points for $\ell/\ell_f \lesssim 1$ either have a large relative error or a large range in the 95 percentile interval in the estimated p_{peak} . For subregions of size $\ell/\ell_f < 1$, determining p_{peak} is subject to large uncertainties ($\gtrsim 20\%$), mostly originating from stochastic variations between the subregions, or low $N_{\text{CC}}(>p_f)$, especially

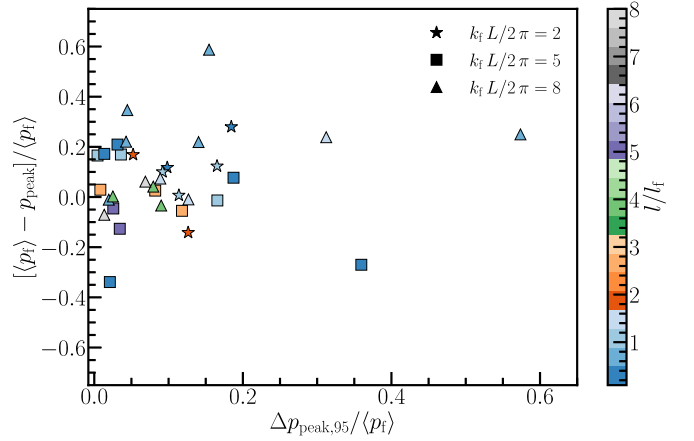


Figure 4. Variation of the relative error on the estimation of p_{peak} , $[(p_f) - p_{\text{peak}}]/(p_f)$, as a function of relative 95 percentile range in p_{peak} , $\Delta p_{\text{peak},95}/(p_f)$, determined from Monte Carlo sampling at 6 GHz. The star, square, and triangle data points represent $k_f L/2\pi = 2, 5,$ and 8 , respectively. Here, $\langle p_f \rangle$ is determined for the entire emitting region. The points are colored based on the subgrid size expressed in ℓ/ℓ_f .

for $k_f L/2\pi = 2$. Hence, even though the overall uncertainties and the 95 percentile range in p_{peak} are mostly within 20% of the $\langle p_f \rangle$, stochastic variations could impact/bias the results for subregions that have size $\ell \lesssim \ell_f$. On the other hand, for $\ell > \ell_f$, both stochastic variation and 95 percentile confidence in p_{peak} are on an average $\lesssim 15\%$ level, and our results can be safely employed.

Note that, for frequencies $\lesssim 1$ GHz, since $N_{\text{CC}}(>p_f)$ is generally larger compared to those at high frequencies (see Figure 1), p_{peak} from the subregions could be determined to have better than 10% accuracy for all k_f s for $\ell \approx \ell_f/2$.

4. Conclusions

Using synthetic p_f maps of synchrotron emission originating due to the action of fluctuation dynamo, we showed that the number of connected polarized structures (N_{CC}) and their filamentarity (F) is a powerful measure to understand the underlying driving mechanism in turbulent, magnetized plasma. $N_{\text{CC}}(>p_f)$ peaks at a certain p_{peak} which is directly related to the $\langle p_f \rangle$ of the entire emitting volume. This is significant because telescope noise in real observations makes the detection of faint polarized emission across the emitting medium difficult, which renders measuring $\langle p_f \rangle$ a challenging task. In such a case, p_{peak} can be used as a measure of $\langle p_f \rangle$ within 10% accuracy. Since p_{peak} lies above ~ 0.1 , a typical level current telescopes can measure in diffuse media. For turbulence driving on scales ranging a factor of 4, p_{peak} can be measured using Minkowski functionals. For systems where turbulence is driven on $\ell_f < L/8$, $p_{\text{peak}} \approx \langle p_f \rangle$ is expected at a lower value (see A. Basu & S. Sur 2021) and likely will not be detectable. However, this will provide an upper limit on p_{peak} .

Intrinsically larger polarized structures on scales comparable to ℓ_f that can be measured at high frequencies ($\gtrsim 3$ GHz) tend to have larger F compared to smaller structures, irrespective of their p_f . However, increasing Faraday depolarization toward low frequencies leads to the breaking up of these large-scale structures into smaller structures with F higher than that of the intrinsic structure. This leads to more ‘‘canal-like’’ structures with $F \approx 1$ and can span over a significant fraction of the emitting medium. Furthermore, these canals span over scales

¹¹ We generated 100 samples from the $N_{\text{CC}}(>p_f)$ versus p_f plot for each subgrid region (similar to Figure 1) by drawing each N_{CC} from a Poisson distribution and estimated p_{peak} by fitting each random sample in the same way as for Figure 1.

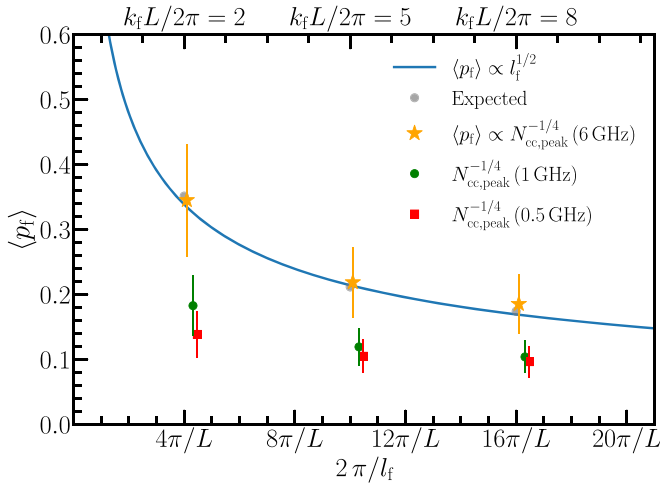


Figure 5. Variation of $\langle p_f \rangle$ with ℓ_f . The gray points show the expected $\langle p_f \rangle$ computed from the magnetic integral scale (ℓ_M), and the blue curve shows the $\langle p_f \rangle \propto \ell_f^{1/2}$ relation, both taken from A. Basu & S. Sur (2021). The red squares, green circles, and yellow stars show $\langle p_f \rangle \propto N_{\text{CC,peak}}^{-1/4}$ at 0.5, 1, and 6 GHz in the presence of Faraday rotation and are plotted with a slight offset in the x-axis to avoid overlap. $N_{\text{CC,peak}}$ are determined from the entire emitting region of the simulated domain.

that are comparable to the turbulence driving. For turbulence driven on small scales, the volume-filling polarized structures are more filamentary. Therefore, high-resolution observations are necessary to understand the origin of turbulence driving in subsonic media.

Since p_{peak} , as measured by N_{CC} over the entire 2D map from the simulated domain, is directly related to $\langle p_f \rangle$, and as shown in A. Basu & S. Sur (2021), at high frequencies, $\langle p_{f,\nu} \rangle \approx \langle p_{f,\text{int}} \rangle$ is related to ℓ_f as $\langle p_{f,\nu} \rangle \propto \ell_f^{1/2}$, we expect N_{CC} to be also important for determining the intrinsic fractional polarization ($\langle p_{f,\text{int}} \rangle$) of an emitting medium. Figure 5 shows the variation of $\langle p_f \rangle$ with $2\pi/\ell_f$, wherein the different symbols show different estimators of $\langle p_f \rangle$. The blue solid curve shows the $\langle p_f \rangle \propto \ell_f^{1/2}$ relation expected from a random walk of polarized emission along the LOS. The yellow stars, green circles and red squares show $N_{\text{CC,peak}}^{-1/4}$ versus $2\pi/\ell_f$, where $N_{\text{CC,peak}}$ corresponds to $N_{\text{CC}}(>p_{\text{peak}})$, and are determined at 6, 1, and 0.5 GHz, respectively. Interestingly, we find $N_{\text{CC,peak}}$ to be an excellent probe of $\langle p_f \rangle$ at higher frequencies, here $\nu = 6$ GHz, where it closely follows the $\langle p_f \rangle \propto \ell_f^{1/2}$ relation. This alludes to an empirical relation $\ell_f \propto N_{\text{CC,peak}}^{-1/2}$. This is not unexpected because the number of components is proportional to the area as $N_{\text{CC,peak}} \propto (L/\ell_f)^2$. Thus, at high frequencies, the number of connected components per unit area of an emitting medium, $N_{\text{CC,peak}}/L^2$, is a direct measure of the number of turbulent cells projected on the plane of the sky.

It is important to highlight that the magnetic integral scale (ℓ_M) varies linearly with ℓ_f (A. Basu & S. Sur 2021). This implies that the variation of $\langle p_f \rangle$ shown in Figure 5 can be equivalently represented in terms of $2\pi/\ell_M$. This will only change the quantitative values in the plot by a scale factor. However, for all practical purposes, comparisons with ℓ_f are more meaningful because of two reasons. First, ℓ_f has a direct connection with the physical mechanism of turbulence driving. Second, while the value of ℓ_M may depend on the Mach number of the flow and the Pm, ℓ_f is a direct input in our simulations, which remains invariant throughout the evolution.

We note that, in order to infer ℓ_f using $N_{\text{CC,peak}}$ discussed above, it is necessary that p_{peak} is well determined. To ensure that the detectable emitting region should be larger than $\sim \ell_f$. In the limiting case, when the region covers an area $\approx \ell_f \times \ell_f$, the inferred p_{peak} would have typical errors up to $\sim 15\%$, which could arise due to a combination of stochastic variation and the accuracy to which p_{peak} can be estimated. However, because of the smaller area, the error on $N_{\text{CC,peak}}$, $\delta N_{\text{CC,peak}}/N_{\text{CC,peak}}$, would roughly scale as $\sqrt{(L/\ell)^2}$, assuming Poisson distribution. A simple back-of-the-envelope calculation suggests that, in an extreme scenario, when $\ell \approx \ell_f$ and $\ell = \mathcal{O}(L/10)$, $\delta N_{\text{CC,peak}}$ is 10 times larger. This would lead to up to a 50% error in the estimated ℓ_f . Although not very accurate, this would provide a realistic estimate of the driving mechanism in the media being studied.

Taken together, our results demonstrate that 2D Minkowski functionals, specifically, the surface density of the number of connected structures obtained from synthetic maps of p_f for $\nu \gtrsim 3$ GHz, are a powerful tool to infer the underlying driving scale of turbulence.

5. Discussion

Our analysis of the Minkowski functionals and N_{CC} relies on detectable polarized emission from a medium where fluctuation dynamo is believed to operate, e.g., in the ICM and in the interstellar medium (ISM) of galaxies. In the context of the ICM, it is to be noted that there is a scarcity of detectable polarized emission in radio halos at present. This is due to the fact that polarized emission in the ICM has been predominantly targeted near 1 GHz. However, as shown in S. Sur et al. (2021) and A. Basu & S. Sur (2021), high-frequency observations at $\nu \gtrsim 3$ GHz are crucial to correctly infer the properties of polarized synchrotron emission arising from Fluctuation dynamo-generated fields. This is because, at these frequencies, the reduction in polarized emission from frequency-dependent Faraday depolarization and beam depolarization are significantly lower compared to that arising due to the steep spectrum of the synchrotron emitting cosmic ray electrons. With this in mind, our analysis of the morphological features at high frequencies presented in this work is a step toward the future, particularly in the light of next-generation radio telescopes when observations using MeerKAT between 2.6 and 3.5 GHz and SKA1-MID between 2.8 and 8.5 GHz would be a reality.

In the ISM of disk galaxies, it is important to note that both large-scale, mean magnetic fields generated by the galactic mean-field dynamo and the turbulent, small-scale magnetic fields generated by fluctuation dynamos coexist, arising from different, albeit related physical mechanisms (R. Beck 2016; A. M. Shukurov & K. Subramanian 2021). In addition to the small-scale fields, polarized emission also originates from large-scale fields on scales $L_{\text{mf}} \gg \ell_f$, where L_{mf} is the scale of the galactic large-scale magnetic field. Thus, the direct use of N_{CC} to infer ℓ_f in the local ISM requires the contribution from the large-scale fields to be isolated. Assuming that resulting polarized emission from large-scale fields is on scales ℓ_{obs} such that $\ell_f < \ell_{\text{obs}} < L_{\text{mf}}$, the contribution from these fields can be removed by subtracting their nonzero $\langle Q \rangle$ and $\langle U \rangle$ determined over an area ℓ_{obs}^2 . Nonetheless, we believe because inferring ℓ_f depends on $N_{\text{CC,peak}}$, which will be dominated by components from turbulent fields, the presence of large-scale fields will not affect it significantly.

Furthermore, because the expected turbulence driving scale in the ISM is $\mathcal{O}(50 \text{ pc})$, physical resolutions of $\approx 10 \text{ pc}$ are needed. With the typical angular resolution of $\sim 2''\text{--}5''$ available from current telescopes, galaxies at distance $\lesssim 2 \text{ Mpc}$, e.g., M31, M33, LMC, IC 10, etc., are the most suitable objects. For Galactic ISM, a careful consideration of diverging LOS with respect to observers on Earth is necessary. A detailed quantification is beyond the scope of this paper and will be addressed elsewhere.

Acknowledgments

R.D. thanks the Indian Institute of Astrophysics (IIA) for support under the Vacation Students Programme (VSP), where ideas of this work germinated. We thank Ancor Damas Segovia for the helpful comments and suggestions. Sharanya Sur acknowledges the use of the High Performance Computing resources made available by the Computer Centre of IIA. We thank the referee for comments that improved the discussion of the results in the paper. The software used in this work was developed in part by the DOE NNSA and DOE Office of Science supported Flash Center for Computational Science at the University of Chicago and the University of Rochester. This work made use of the SCIPY project <https://scipy.org>, NUMPY (C. R. Harris et al. 2020), and ASTROPY:¹² a community-developed core Python package and an ecosystem of tools and resources for astronomy (Astropy Collaboration 2022).

Appendix

Algorithm for Computing Minkowski Functionals

We describe the new algorithm for computing the spatially resolved Minkowski functionals using the Python-based package `perimetrics` (R. Dutta et al. 2024) developed for this work. The two Minkowski functionals, area A and perimeter P , of a 2D structure above a certain threshold value “ p ” are computed from the contour at level p . Since the contours of a gridded map are not smooth (limited by the pixelization) of an otherwise smooth 2D field, our modified algorithm first determines an approximately smooth contour via interpolation. The length of the contour and the area bounded within it give estimates of P and A , respectively. The computation of P and A in our algorithm is based on the *Marching squares* technique of H. Mantz et al. (2008). As described in their work, we directly use the values of the map for determining appropriate contours instead of first converting them into binary maps as done in community-developed Python modules, e.g., `quantimpy` and `scikit-learn`.

However, our implementation differs from H. Mantz et al. (2008) in the following key ways—(i) finding and labeling the connected components so that in the final step, we can simply add the cell-/pixel-wise values of A and P separately for each connected component, and (ii) instead of computing F from the global A and P as performed by H. Mantz et al. (2008), we calculate them separately for each connected component. These have two important advantages. First, our approach reduces the computation complexity from $\mathcal{O}(N^2)$ to $\mathcal{O}(N)$, allows for a robust estimation of F , and retains information on individual connected components for spatially resolved analyses. The second can be readily seen from a simple example. Suppose

that the structures in question are N identical circles with radius R that are isolated from each other, so that the total area $A = N \times \pi R^2$ and the total perimeter, $P = N \times 2 \pi R$. Then, Equation (1) implies $F = (N - 1)/(N + 1) \approx 1$ for large N . Thus, one would erroneously conclude that an image that consists only of circles ($F = 0$) to be highly filamentary.

We illustrate the working of our algorithm using a gray-scale image formed by the superposition of two Gaussians shown in the left panel of Figure 6. Each square pixel in this image is denoted as a “cell” and the corners of the cell as “vertices.” The middle panel in the figure shows the colored labeling of the connected components, while the right panel shows the contours of these connected components. Our *Marching Square* algorithm performs three operations in sequence—(a) segregating regions based on a threshold value and subsequently determining the points through which the contour should pass and assigning A and P values to each cell, (b) identifying and labeling the connected components using the 8-connectivity criteria¹³ (R. C. Gonzalez & R. E. Woods 2002), and (c) combining the component labels with cell-wise A and P values to quantify the area A and the perimeter P in each connected component and subsequently estimate their filamentarity (F). Note that step (a) measures the cell-wise values of A and P as performed by H. Mantz et al. (2008), but it cannot distinguish between separate *structures*. Thus step (b) is essential to identify which pixel belongs to which *structure*. The terms “threshold” and “connected components” carry their usual meanings as used in image processing techniques (see R. C. Gonzalez & R. E. Woods 2002). Further details can be accessed on the Github page of `perimetrics`.¹⁴

A.1. Test of the Algorithm

To test the performance of the algorithm in determining A and P and their errors, we generate smooth, 2D intensity profiles given by,

$$I(r) = 2 - \left(\frac{r}{R}\right)^\alpha. \quad (\text{A1})$$

Here r is the radial distance from the center of the image, and the exponent α determines the gradient (steepness) of the profile at the characteristic radius $r = R$. Note that Equation (A1) implies that the intensity profiles have circular symmetry, and therefore the structure being investigated have circular cross sections that always have $F = 1$.

We set the intensity threshold at a value $I_{\text{thres}} = 1$. This suggests that structures have radius R , and the gradient $\partial I / \partial r = -\alpha / R$ at the edge ($r = R$). The distances are measured in units of the pixel side length. Next, for a given R , we generate a $3R \times 3R$ pixel² image, and the origin, $r = 0$, is defined at the center pixel. Then the connected component for our test cases forms a circle centered at the origin, which spans R pixels between the origin and the edge of the circle. While “ A ” can be approximated quite well at higher resolutions by simply counting the number of cells inside a contour, accurate estimation of “ P ” is sensitive to the details of the contouring

¹³ Let “ S ” represent a subset of pixels in an image. Two pixels “ a ” and “ b ” are said to be *connected* in “ S ” if there exists a path between them consisting entirely of pixels in “ S .” In 2D, this can be obtained either using 4- or 8-connectivity. Thus, for any pixel “ a ” in “ S ,” the set of pixels that are connected to it in “ S ” is called a *connected component* of S .

¹⁴ <https://github.com/rijudutta/perimetrics/tree/main>

¹² <http://www.astropy.org>

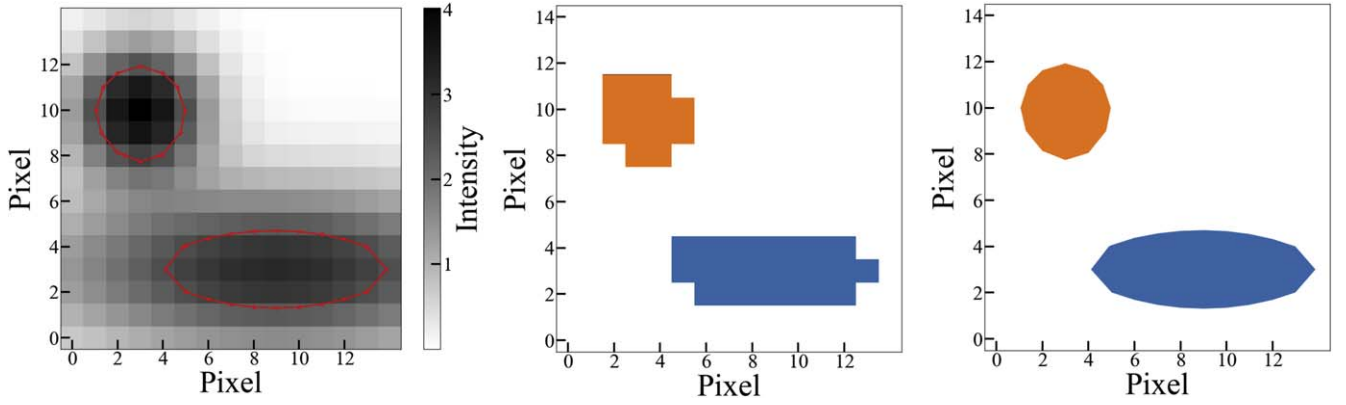


Figure 6. Illustration of the sequence of steps (left to right) performed by our algorithm for a gray-scale image formed by the superposition of two Gaussians. The threshold value of intensity is chosen to be 2.5. The (A, P, F) values obtained for the two connected components shown here are $(12.1, 12.5, 0.01)$ (yellow) and $(25.3, 21.6, 0.2)$ (blue).

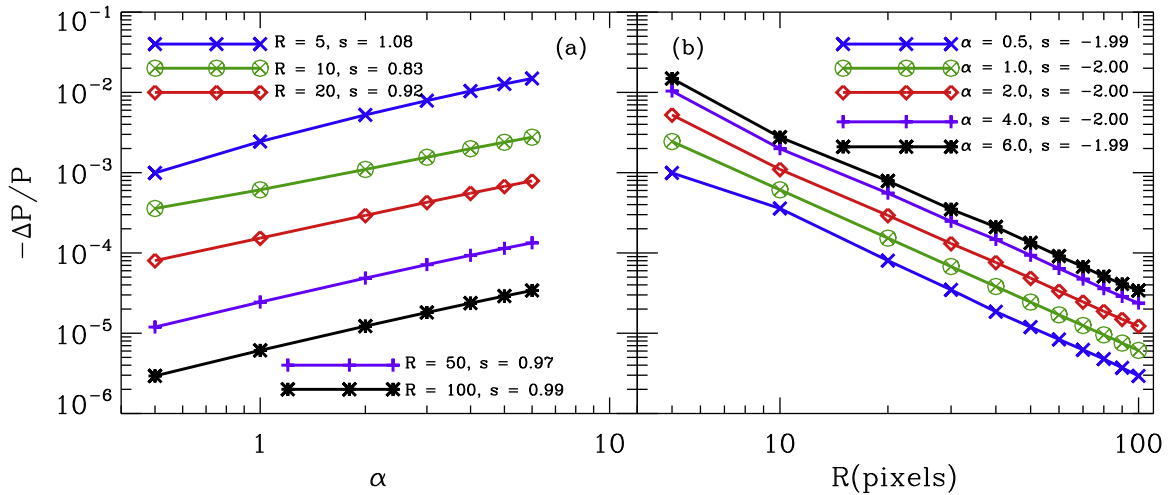


Figure 7. Plots for the fractional error in estimating the perimeter of a circular contour as a function of the exponent α of the power-law intensity profile (left) and the radius R of the circle (right). The gradient of the intensity at the edge of the circle is given by $-\alpha/R$. The values of the slopes “ s ” corresponding to the best linear fits to the curves are shown in the legends.

process. To this end, using our algorithm, we focus on computing P and compare it with the expected value of $2\pi R$.

Figure 7 shows the dependence of the fractional error, $-\Delta P/P = -(P_{\text{comp}} - 2\pi R)/2\pi R$, of the computed value of the perimeter P_{comp} on α (panel “(a)”) and R (panel “(b)”). We find that the error on P decreases with both α and R as a power law. By averaging over the exponents of the respective power laws for a range of α values evenly spaced between 1 and 6, and a range of R values evenly spaced between 10 and 100, we report that the fractional error scales as $\alpha^{0.947}R^{-1.998}$. This suggests a scaling of α/R^2 for the fractional error, which in turn implies that the absolute error in estimating the perimeter, $P - 2\pi R$, is directly proportional to $-\alpha/R$, the gradient of the data at the radius of the contour. Thus, with this code, shallower gradients and higher resolution at the location of the contour lead to a more accurate estimation of the perimeter of the contour.

Moreover, since R is simply the number of pixels across the radius of the circle, the above results indicate that P computed using our algorithm indeed converges to the expected $2\pi R$ as the resolution increases. It is also worth noting from Figure 7 that even at a relatively low resolution, such as $R=5$ (with $\alpha=1$), the fractional error in estimating the perimeter to be -2.4×10^{-3} , while at $R=2$, it is -1.7×10^{-2} . The corresponding fractional errors for area estimation are -8.5×10^{-3}

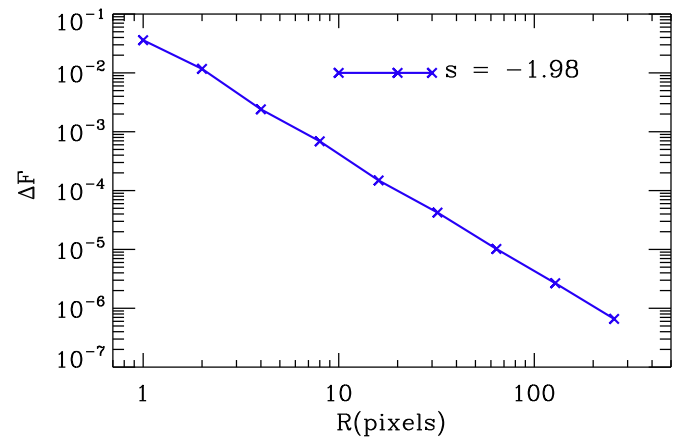


Figure 8. Error in estimating the filamentarity (ΔF) of a circular contour as a function of the radius R of a circle for $\alpha = 1$. Similar to Figure 7, the value of “ s ” corresponding to the best linear fit to the data points is shown in the legend.

and -5.6×10^{-2} respectively. For $\alpha=1$, the error in filamentarity ΔF (equal to the computed F , as the expected $F=0$ for a circle) is shown in Figure 8. We find that $\Delta F \sim R^{-2}$. Note that even for the extreme case of $R=1$, $\Delta F = 0.035$. Larger circles would have even smaller errors in F

as shown in our tests. When compared to mean values of filamentarity, $\langle F \rangle = 0.2 - 0.4$ found in our p_f images, the average error can be expected to be $\lesssim 10\%$ of $\langle F \rangle$.

Thus, the tests indicate that this algorithm can be reliably used to measure morphological quantities of turbulent structures spanning a wide range of sizes, including the smallest resolved structures.

ORCID iDs

Riju Dutta  <https://orcid.org/0009-0000-5591-9063>

Sharanya Sur  <https://orcid.org/0000-0003-4286-8476>

Aritra Basu  <https://orcid.org/0000-0003-2030-3394>

References

- Adler, R. J., & Taylor, J. E. 2007, *Random Fields and Geometry* (New York: Springer).
- Astropy Collaboration 2022, *ApJ*, **935**, 167
- Basu, A., Fletcher, A., Mao, S. A., et al. 2019, *Galax*, **7**, 89
- Basu, A., & Sur, S. 2021, *Galax*, **9**, 62
- Beck, R. 2015, *A&A*, **578**, A93
- Beck, R. 2016, *A&ARv*, **24**, 4
- Benzi, R., Biferale, L., Fisher, R. T., et al. 2008, *PhRvL*, **100**, 234503
- Beresnyak, A. 2012, *PhRvL*, **108**, 035002
- Bharadwaj, S., Sahni, V., Sathyaprakash, B. S., Shandarin, S. F., & Yess, C. 2000, *ApJ*, **528**, 21
- Bhat, P., & Subramanian, K. 2013, *MNRAS*, **429**, 2469
- Calzavari, E., Kerscher, E., Lohse, D., & Toschi, F. 2008, *JFM*, **607**, 13
- Carmo, L., González-Casanova, D. F., Falceta-Gonçalves, D., et al. 2020, *ApJ*, **905**, 130
- Charbonneau, P. 2014, *ARA&A*, **52**, 251
- Cho, J., Vishniac, E. T., Beresnyak, A., Lazarian, A., & Ryu, D. 2009, *ApJ*, **693**, 1449
- Dutta, R., Sur, S., & Basu, A. 2024, perimetrics: v1.0.0, Zenodo, doi:[10.5281/zenodo.11118211](https://doi.org/10.5281/zenodo.11118211)
- Dwivedi, S., Anandavijayan, C., & Bhat, P. 2024, *OJAp*, **7**, 75
- Eswaran, V., & Pope, S. B. 1988, *PhFl*, **31**, 506
- Federrath, C. 2016, *JPIPh*, **82**, 535820601
- Fryxell, B., Olson, K., Ricker, P., et al. 2000, *ApJS*, **131**, 273
- Gaensler, B. M., Haverkorn, M., Burkhart, B., et al. 2011, *Natur*, **478**, 214
- Gonzalez, R. C., & Woods, R. E. 2002, *Digital Image Processing* (Upper Saddle River, NJ: Prentice-Hall)
- Harris, C. R., Millman, K. J., van der Walt, S. J., et al. 2020, *Natur*, **585**, 357
- Haugen, N. E., Brandenburg, A., & Dobler, W. 2004, *PhRvE*, **70**, 016308
- Haverkorn, M., Brown, J. C., Gaensler, B. M., & McClure-Griffiths, N. M. 2008, *ApJ*, **680**, 362
- Hu, Y., Yuen, K. H., & Lazarian, A. 2019, *ApJ*, **886**, 17
- Kalberla, P. M. W., & Haud, U. 2023, *A&A*, **673**, A101
- Kazantsev, A. P. 1968, *JETP*, **26**, 1031
- Mantz, H., Jacobs, K., & Mecke, K. 2008, *JSMTE*, **12**, 12015
- Mao, S., Zweibel, E., Fletcher, A., Ott, J., & Tabatabaei, F. 2015, *ApJ*, **800**, 92
- McKee, C. F., Stacy, A., & Li, P. S. 2020, *MNRAS*, **496**, 5528
- Mecke, K. R., Buchert, T., & Wagner, H. 1994, *A&A*, **288**, 697
- Nandakumar, M., & Dutta, P. 2020, *MNRAS*, **496**, 1803
- Rincon, F. 2019, *JPIPh*, **85**, 205850401
- Sahni, V., Sathyaprakash, B. S., & Shandarin, S. F. 1998, *ApJL*, **495**, L5
- Schekochihin, A. A., Cowley, S. C., Taylor, S. F., Maron, J. L., & McWilliams, J. C. 2004a, *ApJ*, **612**, 276
- Schekochihin, A. A., Cowley, S. C., Taylor, S. F., et al. 2004b, *PhRvL*, **92**, 084504
- Schmalzing, J., & Gorski, K. M. 1998, *MNRAS*, **297**, 355
- Seta, A., Bushby, P. J., Shukurov, A., & Wood, T. S. 2020, *PhRvF*, **5**, 043702
- Seta, A., Federrath, C., Livingston, J. D., & McClure-Griffiths, N. M. 2023, *MNRAS*, **518**, 919
- Seta, A., Shukurov, A., Wood, T. S., Bushby, P. J., & Snodin, A. P. 2018, *MNRAS*, **473**, 4544
- Shukurov, A. M., & Subramanian, K. 2021, *Astrophysical Magnetic Fields: From Galaxies to the Early Universe* (Cambridge: Cambridge Univ. Press)
- Sur, S., Basu, A., & Subramanian, K. 2021, *MNRAS*, **501**, 3332
- Sur, S., & Subramanian, K. 2024, *MNRAS*, **527**, 3968
- Wang, R.-Y., Zhang, J.-F., Lazarian, A., Xiao, H.-P., & Xiang, F.-Y. 2021, *MNRAS*, **505**, 6206
- Wilkin, S. L., Barenghi, C. F., & Shukurov, A. 2007, *PhRvL*, **99**, 134501
- Wittor, D., Brüggem, M., Grete, P., & Rajpurohit, K. 2023, *MNRAS*, **523**, 701
- Xu, S., & Lazarian, A. 2016, *ApJ*, **833**, 215
- Xu, S., & Lazarian, A. 2021, *RvMPP*, **5**, 2